JOURNAL OF AIRCRAFT
Vol. 48, No. 1, January–February 2011

Cavity Flow Assessment Using Advanced Turbulence Methods

Nicholas D. Liggett* and Marilyn J. Smith†
Georgia Institute of Technology, Atlanta, Georgia 30332

DOI: 10.2514/1.C031019

The vortex shedding generated by compressible subsonic flow interacting with a wall cavity has been investigated using large-eddy-simulation-based turbulence techniques embedded within a legacy Reynolds-averaged Navier–Stokes solver. Cavity simulations using hybrid turbulence approaches seek the accuracy of large-eddy simulation by providing filtering and modeling of subgrid-scale turbulence with the cost of traditional Reynolds-averaged Navier–Stokes. Simulations applying differing techniques of hybridization of the Menter k-ω shear stress transport Reynolds-averaged Navier–Stokes approach include detached eddy simulation (DES-SST), blended subgrid-scale turbulence models (GT-HRLES), and a self-adjusting large-eddy-simulation–very-large-eddy-simulation technique (KES) provide an understanding of differing hybrid approaches. Cavity flow results from Reynolds-averaged Navier–Stokes and hybrid simulations are compared with experiment and large-eddy simulation predictions. Evaluation of important flow characteristics illustrates the abilities of these advanced turbulence modeling techniques compared with traditional Reynolds-averaged Navier–Stokes models. Examination of the influence of the grid, time step, and simulation period demonstrates the sensitivity of the aerodynamic and aeroacoustic predictions to these parameters. In particular the subgrid-scale blended model, GT-HRLES, shows significant improvement in the ability to capture the acoustic signatures and flowfield features on a Reynolds-averaged Navier–Stokes or very-large-eddy-simulation grid compared with the other models.

Nomenclature

a_1	=	Menter eddy viscosity parameter
$\arg_2$	=	blending parameter argument for Menter two-equation model
C_l	=	turbulent $(kl)^{\text{sgs}}$ production constant
C_N	=	total normal force coefficient
C_v	=	eddy viscosity constant
c_v	=	constant volume specific heat
$C_{\varepsilon,k}$	=	turbulent kinetic energy dissipation constant
e	=	total energy
e_0	=	internal energy
F_N	=	integrated normal force on the cavity floor
F_2	=	blending parameter for Menter two-equation model
h	=	enthalpy
k	=	kinetic energy
k^{sgs}	=	turbulent kinetic energy
L	=	length of the cavity in the streamwise direction
l^{sgs}	=	subgrid turbulent length scale
M_∞	=	freestream Mach number
n	=	Rossiter mode number
Pr	=	Prandtl number
p	=	pressure
R	=	universal gas constant
res	=	residence periods
S_{ij}	=	strain tensor
S_{ref}	=	reference area for normal force coefficient calculation
SPL	=	sound pressure level, $p_{\text{ref}} = 2.0 \times 10^{-5}$ μPa
T	=	temperature
t	=	physical time
U_∞	=	freestream flow velocity
u_i	=	primitive velocity in the i-direction
$\tilde{u}_i$	=	mass-weighted average flow speed in the i-direction
x_i	=	physical coordinate in the i-direction
y	=	distance to nearest surface
y^+	=	distance to nearest surface in viscous length scales
β_1	=	Menter k-ω shear stress transport inner parameter
β^*	=	Menter k-ω shear stress transport turbulent kinetic energy destruction parameter
γ	=	Rossiter equation empirical parameter
γ_1	=	Menter k-ω shear stress transport turbulent dissipation inner production parameter
Δ	=	grid length scale
δ_{ij}	=	Kronecker delta
κ	=	Menter k-ω shear stress transport parameter, Rossiter equation empirical parameter
μ	=	molecular viscosity
ν	=	kinematic viscosity
ν_t	=	turbulent viscosity
ρ	=	local flow density
ρ_∞	=	freestream flow density
σ	=	viscous work
σ_k	=	Prandtl–Schmidt number for turbulent kinetic energy
σ_{k1}	=	Menter k-ω shear stress transport turbulent kinetic energy inner Prandtl–Schmidt number
σ_{k2}	=	Menter k-ω shear stress transport turbulent kinetic energy outer Prandtl–Schmidt number
σ_{kl}	=	Prandtl–Schmidt number for $(kl)^{\text{sgs}}$
$\sigma_{\omega 1}$	=	Menter k-ω shear stress transport turbulent dissipation inner Prandtl–Schmidt number
$\sigma_{\omega 2}$	=	Menter k-ω shear stress transport turbulent dissipation outer Prandtl–Schmidt number
τ_{ij}	=	resolved stress on the i-face in the j-direction
τ_{ij}^{sgs}	=	subgrid-scale stress on the i-face in the j-direction
ϕ	=	blended k-ω shear stress transport variable

Presented as Paper 2010-1200 at the 48th AIAA Aerospace Sciences Meeting Including the New Horizons Forum and Aerospace Exposition, Orlando, FL, 4–7 January 2010; received 11 March 2010; revision received 22 October 2010; accepted for publication 26 October 2010.

*Graduate Research Assistant and Ph.D. Candidate, Guggenheim School of Aerospace Engineering, 270 Ferst Drive. Member AIAA.

†Associate Professor, Guggenheim School of Aerospace Engineering, 270 Ferst Drive. Associate Member AIAA.

Ψ_t	=	turbulent terms to be linearly combined
Ω	=	absolute value of the vorticity
ω	=	turbulent dissipation

Subscripts and Superscripts

i, j, k	=	tensor directions
sgs	=	subgrid scale
t	=	turbulent
$\overline{(.)}$	=	mean quantity
$\widetilde{(.)}$	=	mass-averaged quantity

I. Introduction

SURFACE cavities where quiescent fluid interacts with a tangential freestream to create a complex flowfield are found in numerous applications. Weapons bays of aircraft, landing gear wells, gaps between lifting surface devices, section juncture gaps, car sun roofs, and open submarine torpedo tubes are just a few examples of cavity flows. Understanding these flows is important as they involve many complex phenomena that may include shear layer instability, flow induced resonance, and turbulence. Vortices leading to strong acoustic oscillations at frequencies which could be potentially damaging to the structure may occur or, if the cavity is part of an aircraft, can result in undesirable noise levels within the cabin. Further understanding of cavity flows may lead to direct potential benefits such as reduced fatigue on structures and lower noise levels.

Cavity flows as diagrammed in Fig. 1 may produce high noise levels when detached shear layers interact with the downstream corner. Dependent upon the ratio of the length of the cavity to the depth, shed vorticity may interact with the downstream corner to produce a feedback loop. Efimtsov et al. [1] found that the unsteady pressure oscillations are related to the Mach number, cavity gap size, cavity depth, and even leading edge radius. The addition of a cavity leading edge radius led to significant reduction in the tones relating to the unsteady pressure oscillations. The step height geometry can also be altered to reduce the Mach number range which gives high intensity tones. Experimental studies [2] have ascertained the unsteady behavior of the shear layer over rearward-facing steps, revealing different modes of behavior for the flow as a function of the cavity length to depth ratio. A random flapping of the shear layer emanating from the upstream corner reattaches to the cavity floor further downstream for longer cavities, while in shorter cavities, this shear layer breaks down into small vortices that can be magnified via Kelvin–Helmholtz instabilities. As the vortices travel downstream, they interact with the downstream corner and travel back upstream through the cavity, resulting in a more unstable, complex flow. The velocity profile of the shear layer of a cavity flow has been examined by Ritchie et al. [3] and the complexity of the flow revealed directly through particle image velocimetry measurements. The greatest streamwise velocities were observed near the cavity corners with the most vorticity occurring near the center of the cavity opening. The importance of the interaction of the cavity flow with the downwind corner has been experimentally confirmed [4], and downstream flow effects observed include larger downstream pressure fluctuations, altered shock locations in supersonic flow, and increased unsteadiness.

Komerath et al. [5] extensively surveyed existing cavity studies in 1987. He classified cavities based on the type of fluid interactions

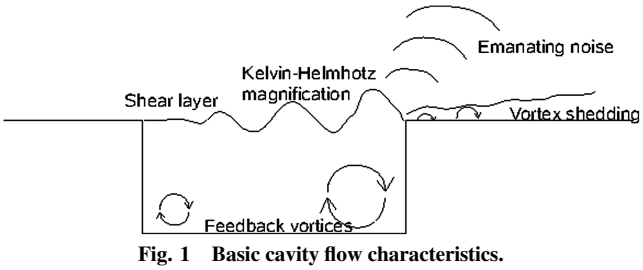

Fig. 1 Basic cavity flow characteristics.

observed in the cavities: fluid dynamic, fluid-resonant, or fluid-elastic. Cavities below a certain size or having a low freestream Mach number were immune from oscillations and resonance. Cavities with oscillations present were categorized based on the modal traits, the frequency in relation to the geometry and Mach number, and boundary or shear layer characteristics. The speed of sound within the cavity was best approximated by the stagnation speed of sound, rather than the free speed of sound, since the temperature recovery factor is generally close to unity, which modifies the frequencies of harmonic modes. Harmonic suppression studies applying passive methods including devices to diminish large eddies, spoilers, cowls, and ramps, or active methods, such as forcing of the shear layer through cavity air injection were also surveyed.

During the past two decades, many computational studies have been devoted to cavity flows, ranging from Reynolds-averaged Navier–Stokes (RANS) with algebraic turbulence models to direct numerical simulations (DNS). A number [6–10] of these studies have focused on the evaluation of various mechanisms to reduce noise sources. Earliest simulations involved the application of RANS methods, and indeed their relative low cost continues to make them appealing. Tam et al. [11] analyzed cavity flows using the algebraic Baldwin–Lomax turbulence model with different modifications such as upstream relaxation, the Degani–Schiff first mode modification, and the multiple-wall model. Through this study, he evaluated the performance of different Baldwin–Lomax modifications though their reproduction of cavity flow characteristics, dissipation, mode frequency identification, and sound pressure levels, although he noted that no model produced acceptable results in all of the categories. Using the Baldwin–Lomax model, the reflected vortices from the downstream corner dissipated before reaching the upstream wall, and in the process secondary vortices were created deeper in the cavity, completing the cycle of feedback. Time-averaged sound pressure levels at the cavity floor center as low as 151 dB and as high as 169 dB were observed as a result of this feedback. Shrinivasan and Baysal [6] also employed a Baldwin–Lomax algebraic turbulence model to examine the instantaneous and time-averaged characteristics of a compressible, subsonic flow over a cavity. The time-averaged results were promising; however, they failed to accurately reproduce the flow and aeroacoustics occurring at the floor and rear face of the cavity. Computational fluid dynamics (CFD) cavity studies with a two-equation k-ω turbulence model [7] in low supersonic freestream Mach numbers confirmed the ability of RANS to capture large scale structures present in experiment, but while the method resulted in surface pressures with the characteristic harmonic modes of cavity flows, large errors in the mode amplitudes were apparent, and higher frequency harmonics were suppressed. A second CFD study [12] using the two-equation k-ω turbulence model more accurately reproduced sound pressure levels on the downstream wall than the two-dimensional results, though the levels were still consistently over predicted in both cases. The inadequate performance of these RANS simulations can likely be attributed to the inability of the turbulence models to capture the unsteady effects and small scale structures of the flow, not unexpected as RANS turbulence models are statistical representations of time-averaged flows.

At the other end of the cost spectrum are DNS in which no turbulence model exists, but instead an extremely fine computational mesh is used to capture all of the turbulence characteristics down to the Kolmogorov scales. This method has resulted in the identification of the sources of instability for two- and three-dimensional cavity configurations [13]. The capabilities of DNS to resolve the complex physics of cavities are mitigated by the computational constraints for spatial and temporal resolution, resulting in a limited engineering applicability given current computational resources.

A less costly alternative to DNS is the use of large-eddy simulations (LES), where the larger turbulence eddy scales are resolved, and turbulence modeling is employed at scales that are smaller than the grid (i.e., subgrid-scales). The smaller turbulence scales are assumed to be more isotropic and contain less turbulent energy, leading to fewer sources of error than a comparable RANS solution. Several recent efforts [8,9,14,15] that have applied LES to

cavity flows have recently been published. Levasseur's transonic cavity simulations [8] illustrate the ability of LES to capture the Rossiter frequencies at the cavity floor center. Thornber's deep cavity LES simulations [9] also produced flowfields and sound pressure levels that correlated very well with experiment. Additional LES studies solving a form of the lattice-Boltzmann equation on small aspect ratio cavities [14] included deep cavities and cavities with overhangs. Deep cavities revealed a dual vortex structure, with a strong vortex in the deeper part of the cavity. These simulations could be performed at only moderate Reynolds numbers due to computational cost, a significant problem with pure LES simulations.

Unconventional cavity geometries have also been examined using LES methods. Mincu et al. [15] has carried out LES studies for a cavity having a circular cross section to ascertain the sound development and subsequent radiation from a cavity flow. As with the rectangular cavity cases, discrete frequencies dominated the acoustics, but wind tunnel installation effects were the most important factor. Drag increase due to the cavity was also examined in the circular cavity studies. All studies mentioned previously were for subsonic or low transonic regimes. Other LES studies have also attempted to model the important acoustics that occur in the supersonic regime over rectangular cavities [16], to develop a model to correlate the change in frequency with change in cavity aspect ratio and Mach number.

Given the relatively high computing cost of LES, interest in recent years has focused on the development of hybrid RANS-LES turbulence methods that can be applied to both less refined [RANS/very-large-eddy-simulation (VLES)] and more refined (LES) grids. Syed applied a detached eddy simulation (DES) with the Spalart–Allmaras RANS model (SA-DES) on cavity flows [17] and observed that modes in the sound pressure levels were predicted much better than with traditional RANS simulations. SA-DES was also applied by Mahmoudnejad and Hoffmann [18] on a three-dimensional cavity, producing good experimental agreement of the mean pressures along the cavity floor. A comparison of SA-DES and hybrid RANS/LES using the two-equation k-ε model [19] for cavity flows demonstrated the ability of DES to generate results similar to LES using an order of magnitude fewer grids points. Li and Hamed's [20] focus on the effect of the wall boundary conditions on the flowfield acoustics used a hybrid method with a low cost RANS model in the attached flow region and LES in the separated region. The authors found that an inviscid sidewall boundary condition produced better results with the hybrid simulations than a periodic sidewall boundary condition.

This study examines a transonic flow over a rectangular cavity with a moderate size grid comparable to RANS or VLES computations, correlating the predictions of several hybrid turbulence techniques with experiments and other simulations. The highly unsteady nature of the flow with strong vortex shedding and large degrees of separation may lead to smearing of the flow characteristics using traditional RANS turbulence methods, as noted in the prior studies discussed. Previous cavity studies have used DES-based methods, while here hybrid RANS-LES blended with the Menter k-ω shear stress transport (SST) RANS model (GT-HRLES) and LES-VLES hybrid (KES) methods are evaluated for frequencies below 500 Hz. It is important to note the the differences in these hybrid approaches. The hybridization of DES provides a single model that acts in a traditional RANS manner near the wall, and provides a filtering approach, which is grid dependent, for subgrid-scale modeling in the separated regions [21,22]. The DES-SST method is applied in this study, but differs from additional methods also studied in this work, which provides blending of the RANS turbulent kinetic energy with an LES subgrid-scale model. The addition of KES simulations provides a differing technique by modeling transport of kinetic energy and an energy/length scale term, rather than dissipation. Each hybrid approach illuminates sources of differences and applicability of the models through the results. Previous successful LES cavity studies [8,14,15,20] lend credence that LES turbulence methods with subgrid-scale models merged into legacy RANS codes may provide similar success with fewer computational resources.

II. Experiment Correlation

The generic cavity rig used by QinetiQ for a set of cavity experiments [23] was chosen as the correlation configuration in this study. These experiments have also formed the basis for correlation by a number of computational simulations [8,17,18,24] using LES and DES with Spalart–Allmaras, k-ω SST, and k-ε turbulence models. Each computational study has examined the mean or unsteady pressure at one or more locations along the cavity floor.

The cavity was embedded in a rig mounted on a sting, and the pressures across the cavity floor were monitored in at various freestream steady flows. The experimental study varied the depth of a rectangular cavity having a length of 0.508 m and a width of 0.1016 m. Shallow (0.0508 m) and deep (0.1016 m) cavities were examined. No cavity motion, inclination, or yaw was considered. The rig had a length of 1.8288 m with the leading edge of the cavity located at 0.7874 m, and a width of 0.4318 m with the cavity centerline offset by 0.0254 m from the rig centerline. Pressure measurements were taken using static pressure transducers along the cavity floor at 10 locations and the rig at 28 and 14 locations ahead and aft of the cavity, respectively. Mach numbers of 0.6, 0.85, and 1.35 were studied with total pressures ranging from 101.65 to 102.55 kPa and total temperatures from 302.32 to 311.35 K.

For comparison with the results from other computational studies, this work evaluated the deep cavity (5:1:1) at a Mach number of 0.85 near sea-level standard atmospheric conditions with a total pressure of 101.65 kPa, total temperature of 302.32 K, and Reynolds number of 1.38×10^7. The static temperature from isentropic relations is then 263 K, resulting in a flow speed of 276 m/s. Although data are available at multiple axial stations, results are compared at only station K23. Comparisons at multiple stations would give additional data, but may detract from the clarity of the application of multiple turbulence models.

III. Computational Setup

The simulations were performed using the OVERFLOW 2.1z [25] flow solver. A fourth-order central-difference Euler scheme resolved the spatial flowfield, while a second-order temporal integration scheme was achieved via a diagonalized beam-warming scalar pentadiagonal algorithm with Newton subiterations. After evaluation of the different artificial viscosity schemes within the code to determine which was the least dissipative, numerical viscosity to stabilize the scheme was added in the form of a fourth-order generalized thin-layer Navier–Stokes dissipation scheme. This dissipation scheme adds smoothing to ρh_0 in the form of dissipation coefficients to the second- and fourth-order discretization of the spatial derivatives. Based on computational evaluations, second and fourth-order dissipation coefficients of 2.0 and 0.04, respectively, were the minimum values that provided stability without overly dissipating the features of the cavity flowfield.

The fluid composition assumes air is a perfect gas having a constant ratio of specific heats of 1.4. The cavity simulations were computed with dimensional time steps ranging from as small as 3.62×10^{-6} to as large as 2.00×10^{-5} seconds for total simulations time ranging from 0.0663 to 0.5000 s. The smallest period is equivalent to a fluid element traveling 36.6 grid lengths or *residence periods*, whereas the longest period is equivalent to 276 residence periods. Explicitly, a single residence period is defined as

$$t_{\text{residence}} = \frac{L}{U_\infty} \tag{1}$$

A freestream turbulence intensity of 10% and normalized turbulent kinetic energy of 10^{-6} were prescribed to initialize the simulation.

A. Grid

Two-dimensional slices of the cavity grid are presented in Figs. 2a and 2b, respectively. This grid, referred to as grid 2R, has outer boundaries that correspond to Levasseur's M3 LES grid [8]. An

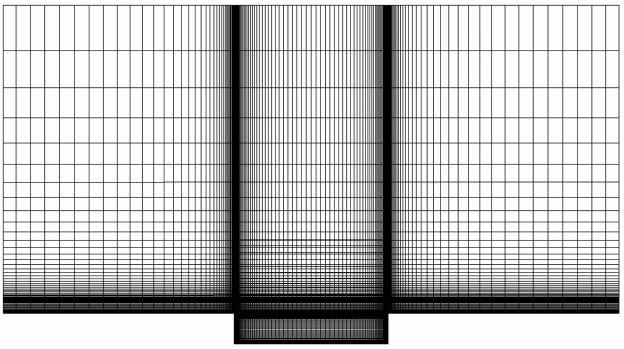

a) Overall view of the cavity and external flow grids

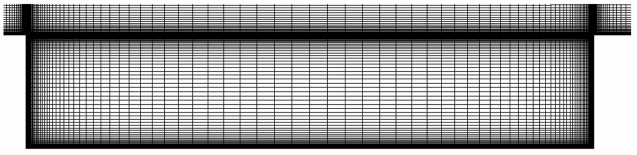

b) Cavity grid close-up

Fig. 2 Cavity grid profile view.

overset approach has been applied with a refined grid to model the internal cavity with a second mesh to model the area external to the cavity. The cavity grid extends 0.2422 m into the flowfield grid and applies an overset approach to exchange information between the grids. There are 161 grid points along the length of the cavity, 188 grid points from the cavity floor to the overset boundary, with 73 of those grid points overlapping the flowfield grid, and 115 grid points across the cavity width. Stretching and spacing between the cavity and external flow grids are matched for the overlap boundary at the cavity opening.

The area (and grid) external to the cavity is 2.032 m (297 points) in the streamwise direction, 0.6096 m (241 points) in the spanwise direction, and 1.016 m (95 points) in the direction normal to the external wall. The middle of the cavity opening is in the middle of the bottom external flow wall as seen in the grid orthogonal view in Fig. 3. The initial grid spacing normal to the wall for both grids is 3.0×10^{-6} m, yielding a viscous grid spacing of $y^+ < 1.0$ at the wall. The wall and internal cavity surfaces are viscous and modeled as adiabatic boundary conditions with pressure extrapolation. The inflow and outflow conditions employ Reimann invariants consistent with the work of other authors [26], and as this study aims to produce results on par with previous LES studies by other authors, similar boundary conditions [8,17,24,27] were desired. The two side boundaries corresponding to the width axis of the cavity were treated as symmetry planes. The overset boundaries between the two grids were interpolated with three fringe points.

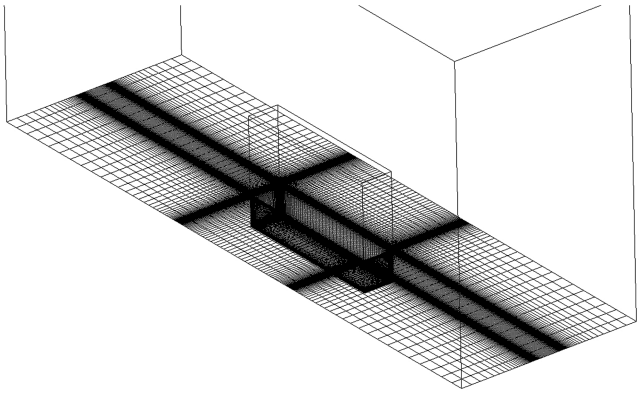

Fig. 3 Cavity grid orthogonal view.

B. Turbulence Simulation Techniques

The fully compressible mass, momentum, energy, and turbulence transport equations are solved using an implicit finite-differencing scheme and integrated in a time-accurate manner with the fully viscous Navier–Stokes flow solver OVERFLOW [25]. OVERFLOW uses an overset grid approach where structured grids are used to simulate complex geometries, allowing one to combine body-fitted near-body grids with background grids to cover the entire domain of interest. This approach gives the simplicity of a structured solver with complex geometries that would normally demand use of an unstructured solver, requiring more programming and memory overhead. At physical features such as viscous walls or far-field inlets, conventional boundary conditions are used. For the case of overlapping grids, interpolation between the edge nodes of the grids gives the conserved field variables. OVERFLOW is capable of time-accurate simulations of complex geometries with many elements that may move relative to each other with any desired motion. Internal and external flows may be investigated.

The governing equations solved by OVERFLOW [28] are outlined. The Navier–Stokes equations may be written in vector form with respect to a generalized coordinate system as

$$\frac{\partial q}{\partial t} + \frac{\partial \mathbf{E}}{\partial \xi} + \frac{\partial \mathbf{F}}{\partial \eta} + \frac{\partial \mathbf{G}}{\partial \zeta} \tag{2}$$

The generalized coordinates are ξ, η, and ζ, whereas the fluxes in each direction are $\mathbf{E}$, $\mathbf{F}$, and $\mathbf{G}$. The vector of conserved scalars is

$$\frac{\mathbf{q}}{V}\begin{bmatrix} \rho \\ \rho u_1 \\ \rho u_2 \\ \rho u_3 \\ \rho e_0 \end{bmatrix} \tag{3}$$

Here, ρ, u_i, p, and e are the unknown field variables of density, velocity in each of the three directions, pressure, and total energy per unit mass, respectively. The control size is V. These equations are linearized and a pseudotime term is added to allow subiteration and faster iterative numerical schemes to be employed. The resulting system is

$$\left[I + \frac{\Delta t}{(1+\theta)\Delta\tau} + \frac{\Delta t}{1+\theta}(\partial_\xi A + \partial_\eta B + \partial_\zeta C)\right]\Delta q^{n+1,m+1} = \tag{4}$$

$$-\left[(q^{n+1,m} - q^n) - \frac{\theta}{1+\theta}\Delta q^n + \frac{\Delta t}{1+\theta}\mathrm{RHS}^{n+1,m}\right] \tag{5}$$

To provide second-order temporal accuracy $\theta = 1/2$ is used in this study. The fluxes create the right-hand side term as

$$\mathrm{RHS} = \frac{\partial \mathbf{E}}{\partial \xi} + \frac{\partial \mathbf{F}}{\partial \eta} + \frac{\partial \mathbf{G}}{\partial \zeta} \tag{6}$$

With five equations in six unknowns, a state equation is needed to close the system. Using the perfect gas assumption, the internal energy per unit mass can be related to the temperature by

$$e_0 = c_v T \tag{7}$$

The proportionality constant is c_v, the specific heat at constant volume. The internal energy per unit mass is now related to the total energy per unit mass using Einstein notation for repeated indices by

$$e = e_0 + \frac{1}{2}u_k u_k \tag{8}$$

Finally, the system of equations is now closed using the state relation

$$p = \rho R T \tag{9}$$

This is a system of six equations in six unknowns. The system could be solved with no further analysis using discretization methods

with appropriate integration and boundary conditions. Unfortunately, such an approach would likely lead to the need of tremendous amounts of computer resources for even the smallest of solution domains to capture the physics of the flow. As such, the turbulent length scales are split into resolved and unresolved regimes. The resolved portions may be solved as usual with a grid fine enough to reproduce the flow features, while the unresolved parts may be modeled to reduce computational requirements of the problem. The unresolved subgrid-scale stresses use an eddy viscosity model and are calculated from

$$\tau_{ij}^{\text{sgs}} = 2\bar{\rho}\nu_t\left(\tilde{S}_{ij} - \frac{1}{3}\tilde{S}_{kk}\delta_{ij}\right) - \frac{2}{3}\bar{\rho}k^{\text{sgs}}\delta_{ij} \tag{10}$$

The turbulent eddy viscosity, ν_t, and the turbulent kinetic energy, k^{sgs}, are calculated using one of several turbulence approaches.

These are the equations that are solved by OVERFLOW. In addition to the Navier–Stokes equations, OVERFLOW has the capability of using any one of a number of turbulence techniques, including no turbulence modeling, algebraic model, one-equation models, and two-equation models. This study focuses on the two-equation approaches available in OVERFLOW.

1. Menter k-ω SST Approach

The first turbulence approach is available as an option in the unmodified OVERFLOW code. This technique is the Menter k-ω SST two-equation turbulence model [29], developed as an alternative to the standard k-ω model [30], which transports the turbulent kinetic energy and turbulent dissipation using the following transport equations:

$$\frac{\partial \rho k}{\partial t} + \frac{\partial \rho u_j k}{\partial u_j} = \tau_{ij}\frac{\partial u_i}{\partial x_j} - \beta^*\rho\omega k + \frac{\partial}{\partial x_j}\left[(\mu + \sigma_k\mu_t)\frac{\partial k}{\partial x_j}\right] \tag{11}$$

$$\frac{\partial \rho\omega}{\partial t} + \frac{\partial \rho u_j \omega}{\partial u_j} = \frac{\gamma}{\nu_t}\tau_{ij}\frac{\partial u_i}{\partial x_j} - \beta\rho\omega^2 + \frac{\partial}{\partial x_j}\left[(\mu + \sigma_\omega\mu_t)\frac{\partial \omega}{\partial x_j}\right] + 2(1-F_2)\rho\sigma_{\omega 2}\frac{1}{\omega}\frac{\partial k}{\partial x_j}\frac{\partial \omega}{\partial x_j} \tag{12}$$

The constants are calculated by the blending function, ϕ, where

$$\phi = F_2\phi_1 + (1-F_2)\phi_2 \tag{13}$$

and the blending parameter is

$$F_2 = \tanh(\arg_2^4) \tag{14}$$

$$\arg_2 = \max\left(2\frac{\sqrt{k}}{0.09\omega y}; \frac{500\nu}{y^2\omega}\right) \tag{15}$$

where y is the distance to the nearest viscous surface. The turbulent eddy viscosity is computed from

$$\nu_t = \frac{a_1 k}{\max(a_1\omega; \Omega F_2)} \tag{16}$$

where Ω is the absolute value of the vorticity with $a_1 = 0.31$. The SST set 1 inner variables are set to $\sigma_{k1} = 0.85$, $\sigma_{\omega 1} = 0.5$, $\beta_1 = 0.0750$, $\beta^* = 0.09$, and $\kappa = 0.41$. The turbulent dissipation inner production parameter is

$$\gamma_1 = \frac{\beta_1}{\beta^*} - \sigma_{\omega 1}\frac{\kappa^2}{\sqrt{\beta^*}} \tag{17}$$

The outer layer constants include $\sigma_{k2} = 1.0$, $\sigma_{\omega 2} = 0.856$, $\beta_2 = 0.0828$, $\beta^* = 0.09$, and $\kappa = 0.41$. The turbulent dissipation outer production parameter is computed as

$$\gamma_2 = \frac{\beta_2}{\beta^*} - \sigma_{\omega 2}\frac{\kappa^2}{\sqrt{\beta^*}} \tag{18}$$

2. DES Approach (DES-SST)

The DES approach, available in the unmodified OVERFLOW code [31], relies on a redefinition of the length scale used in the Menter SST equations for dissipation of the turbulent kinetic energy. The length scale of the SST model in terms of the transport variables is

$$l = \frac{k^{\frac{1}{2}}}{\beta^*\omega} \tag{19}$$

The redefined DES length scale is

$$l_{\text{DES}} = \min[l, C_{\text{DES}}\max(\Delta x, \Delta y, \Delta z)] \tag{20}$$

Here, C_{DES} is blended using the Menter blending function, where $C_{\text{DES}_1} = 0.78$ and $C_{\text{DES}_2} = 0.61$. This new definition alters the turbulent kinetic energy dissipation term from $D^k = \rho\beta^* k\omega = \rho k^{3/2}/l$ to $D^k = \rho k^{3/2}/l_{\text{DES}}$. The effect of this change is an increase in the turbulent kinetic energy dissipation in regions where the grid size is smaller than the estimated turbulent length scales, allowing the solver to resolve rather than model larger eddies.

3. Hybrid RANS-LES Approach (GT-HRLES)

The GT-HRLES [32] and DES-SST techniques both employ the Menter k-ω SST base model, but use differing approaches for the unresolved turbulence. The GT-HRLES method uses the subgrid length scale as a filter and explicitly blends the kinetic energy of the two-equation SST model with a one-equation subgrid-scale kinetic energy model using the Menter blending function. This differs from the DES-SST method which redefines the length scale as a filtering method, but uses the Menter equations to perform this subgrid modeling. The GT-HRLES approach was added to OVERFLOW 2.0y by Shelton et al. [33] and originally relied on a DES-like assumption. This work extends the implementation to include the subgrid-scale turbulence model. Beginning with the Menter two-equation k-ω SST formulation as given in Eqs. (11) and (12) for the transport of turbulent kinetic energy and dissipation, respectively, the addition of a an LES turbulent kinetic energy equation gives

$$\frac{\partial \bar{\rho}k^{\text{sgs}}}{\partial t} + \frac{\partial \bar{\rho}\tilde{u}_i k^{\text{sgs}}}{\partial u_i} = \tau_{ij}^{\text{sgs}}\frac{\partial \tilde{u}_i}{\partial x_j} - C_\varepsilon\bar{\rho}\frac{(k^{\text{sgs}})^{3/2}}{\bar{\Delta}} + \frac{\partial}{\partial x_i}\left[\bar{\rho}\left(\frac{\nu}{Pr} + \frac{\nu_t}{Pr_k}\right)\frac{\partial k^{\text{sgs}}}{\partial x_i}\right] \tag{21}$$

Here, the eddy viscosity is

$$\nu_t = C_\nu\bar{\Delta}\sqrt{k^{\text{sgs}}} \tag{22}$$

The length scale is

$$\bar{\Delta} = (\Delta x\Delta y\Delta z)^{\frac{1}{3}} \tag{23}$$

The turbulent terms of the Menter k-ω SST and the LES turbulent kinetic energy terms may be linearly combined [34] to form

$$\Psi_t = F_2\Psi_t^{\text{RANS}} + (1-F_2)\Psi_t^{\text{sgs}} \tag{24}$$

The blending function F_2 is defined in Eqn. (14).

4. LES-VLES Approach (KES)

The last addition to OVERFLOW is the LES-VLES (KES) turbulence technique, developed by researchers at Georgia Tech [35,36] and originally implemented in the OVERFLOW 2.0y code by Shelton et al. [33], which resolves two k and kl turbulence equations, and provides an approach that adjusts and may resolve scales when grids are employed in Direct Numerical Simulation up to VLES. This approach differs from the other approaches in that it

Table 1 Grid solution convergence with varying initial normal wall spacings

Wall spacing, m	Wall shear stress, Pa	Viscous wall spacing
3.0×10^{-2}	0.8	351.7
3.0×10^{-3}	5.9	96.3
3.0×10^{-4}	44.0	26.3
3.0×10^{-5}	69.0	10.3
3.0×10^{-6}	86.7	0.92
3.0×10^{-7}	87.3	0.11

directly calculates the length scale, rather than relying on the grid spacing. The Favre filtered transport equations are for the subgrid k^{sgs} and $(kl)^{\text{sgs}}$ are

$$\frac{\partial \bar{\rho} k^{\text{sgs}}}{\partial t} + \frac{\partial \bar{\rho} \tilde{u}_i k^{\text{sgs}}}{\partial u_i} = \tau_{ij}^{\text{sgs}} \frac{\partial \tilde{u}_i}{\partial x_j} - C_{\varepsilon,k} \bar{\rho} \frac{(k^{\text{sgs}})^{3/2}}{l^{\text{sgs}}} + \frac{\partial}{\partial x_i}\left[\bar{\rho}\left(\frac{\nu}{Pr} + \frac{\nu_t}{\sigma_k}\right)\frac{\partial k^{\text{sgs}}}{\partial x_i}\right] \tag{25}$$

$$\frac{\partial \bar{\rho}(kl)^{\text{sgs}}}{\partial t} + \frac{\partial \bar{\rho} \tilde{u}_i (kl)^{\text{sgs}}}{\partial u_i} = C_l l^{\text{sgs}} \tau_{ij}^{\text{sgs}} \frac{\partial \tilde{u}_i}{\partial x_j} - C_{\varepsilon,kl} \bar{\rho} (k^{\text{sgs}})^{3/2} + \frac{\partial}{\partial x_i}\left[\bar{\rho}\left(\frac{\nu}{Pr} + \frac{\nu_t}{\sigma_{kl}}\right)\frac{\partial (kl)^{\text{sgs}}}{\partial x_i}\right] \tag{26}$$

These equations give the subgrid velocity scale, $(k^{\text{sgs}})^{1/2}$, and the subgrid length scale l^{sgs}. The constants used for these equations are set to $C_{\varepsilon,k} = 0.916$, $C_l = 1.06$, $\sigma_k = 0.9$, $\sigma_{kl} = 2$. The dissipation coefficient for $(kl)^{\text{sgs}}$ is

$$C_{\varepsilon,kl} = 0.58 + 2\frac{C_\nu}{\sigma_{kl}}\left(\frac{\partial l^{\text{sgs}}}{\partial x_j}\right)^2 \tag{27}$$

where the eddy viscosity constant is $C_\nu = 0.0067$.

IV. Results

The results of the simulations are compared in terms of the aeroacoustic properties and convergence characteristics of integrated cavity floor pressures. The aeroacoustic behavior for the cavity has been determined by applying Fourier transforms to the pressure data at the cavity floor center. The mode frequencies and amplitudes for each turbulence technique are recorded from the transformed data and compared with experimental values via relative errors. For the experimental data [23], unsteady pressure information was gathered at sensor locations using Kulite pressure transducers with the data determined to an uncertainty of 12 Hz. The data are also compared with the Rossiter frequency modes [37]:

$$f_n = \frac{U_\infty}{L}\frac{n - \gamma}{M_\infty + 1/\kappa} \tag{28}$$

The reference velocity, U_∞, and reference Mach number, M_∞, are the freestream velocity and Mach number, respectively, that correspond to $U_\infty = 276$ m/s and $M_\infty = 0.85$ for this study. The reference length, L, is the streamwise cavity dimension of 0.508 m. The parameters γ and κ are provided from experimental results with κ set typically to 0.57, while γ varies between 0 for a deep cavity and 0.57 for a shallow cavity. The desired mode is calculated by setting n equal to the mode number. A value of $\gamma = 0.307$ is applied in this work to permit direct comparison with Levasseur et al. [8]. A reference pressure of 2.0×10^{-5} Pa is used for calculation of sound pressure levels.

A. Grid Spacing Study

The influence of grid spacing on the simulations was examined via initial normal wall spacings with a rate of expansion of less than 15% to identify the normal and length spacing (the spacing in the direction of the width was constant). The largest aspect ratio at the wall varied from 0.128 for the coarsest normal spacing up to 12,800 for the finest normal spacing. The wall spacing was varied from 3.0×10^{-2} to 3.0×10^{-7} m, resulting in refined grid. For each case, the wall stress was calculated from the gradient of the flow at the wall. Convergence of the shear stress was used as a criterion for the minimum necessary initial normal wall spacing in Table 1. With a shear stress change of 0.7% between the two finest spacings, an initial normal spacing of 3.0×10^{-6} is considered converged.

The grid setup used here is compared with other works such as a study by Allen and Mendonca [24] which has $y^+ < 300$, and simulations by Syed and Hoffmann [17] which have $y^+ < 2$. It is clear that a large viscous spacing near 300 at the surface will not properly capture the surface physics; however, the viscous spacing near 2 may properly reproduce the near-wall flow. The average grid spacing of the different setups is similar where Allen, Syed, and this study have mesh spacings of 1.89×10^{-2}, 1.56×10^{-2}, 1.64×10^{-2} m, respectively, within the cavity.

B. Influence of the External Grid Domain

Experimental investigations of cavities, such as [4] have noted the interaction of the cavity with the downstream external flow. In subsonic freestream configurations, this interaction may influence the cavity behavior, and the numerical control volume should be large enough to capture these potential interactions. To examine the influence of the external grid domain on the analysis, two meshes with different far-field boundary locations (Table 2) were evaluated, similar to the analysis by Levasseur et al. [8]. The cavity dimensions and grid remained constant for this study. The number of mesh points used in the external grids were not altered between grid 1R and grid 2R. The simulations performed by Levasseur et al. [8] differ somewhat from this study as Levasseur employed unstructured grids, whereas grids 1R and 2R are structured grids. The unstructured meshes in the study by Levasseur have 3×10^6 elements for the coarse M1 mesh and 9×10^6 elements for the fine M3 mesh. The physical dimensions of Levasseur's meshes M1 and M3 are the same as grids 1R and 2R, respectively, from Table 2. In the LES study by Levasseur et al. [8], M1, the smaller domain grid, does not obtain as high a quality solution as the larger domain grid, and similar conclusions have been observed here using the hybrid RANS/LES method. The pressure histories for the two simulations in Fig. 4 illustrate that the pressure oscillations predicted in mesh 1R have a lower amplitude and higher frequency than those oscillations found in the 2R pressure history.

The influence of the extent of the external domain can also be observed on the harmonics of the pressure at the midpoint of the cavity floor (Table 3). The mode frequencies are compared with experimental values which have an error of 12 Hz. This error corresponds to 3.4% of the total for the low frequency mode 2 and 1.4% of the total for the high frequency mode 4. While the current simulation using the smaller extent grid has about 1/3 of the LES error for mode 2, the errors at higher harmonics are 3–5 times larger than the errors of the LES simulation. The smaller domain

Table 2 Grid comparisons for small and large grid domains

Grid	Streamwise, m, nodes	Spanwise, m, nodes	Height, m, nodes
1R, External Flow	1.3208, 297	0.4064, 241	1.016, 95
2R, External Flow	2.0320, 297	0.6096, 241	1.016, 95
1R and 2R, Cavity	0.508, 161	0.1016, 115	0.1016, 115
——	——	——	+0.1406 overset, +73

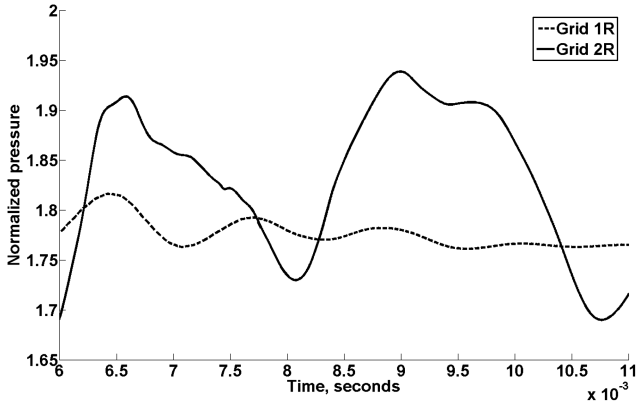

Fig. 4 Pressure history at the cavity floor center for the smaller flowfield cavity setup.

simulations using both LES and hybrid RANS/LES methods result in errors up to 25–30% compared with the experimental values. The larger domain M3 mesh results are also listed in Table 3, which demonstrate that the errors for the current simulations are of the same order as the LES simulations, even with the smaller mesh sizes that correspond to RANS/VLES level simulations. While the LES predictions have the largest improvement for the lowest mode with the M3 mesh, the GT-HRLES results show the most improvement at the higher modes.

Data are not available for mode 1, as a much longer simulation is required to accurately capture lower harmonics, and for many applications the higher harmonics are of more interest. The increase in the outer domain size from the close far-field mesh 1R to the distance far-field mesh 2R can result in a drop in error in the prediction of the mode frequencies of an order of magnitude, validating the use of a larger and more costly grid domain. The predictions using the 1R grid do not fall within the experimental error bounds of 12 Hz, however, the predictions using the 2R grid fall within these error bounds. These results indicate a strong sensitivity to boundary condition contamination for a small domain using these hybrid and URANS methods, similar to the findings of Levasseur et al. [8] for LES methods.

C. Spectral Estimation

The desire to properly capture acoustics within the flow necessitates an analysis of the approaches employed to determine the frequency spectrum. The cavity LES work of Levasseur et al. [8] employed the Burg method of spectral estimation [38,39] in determining the sound pressure levels within the cavity, rather than traditional fast Fourier transform (FFT). This method has been used in other studies [40,41] with the desired of improving the power spectrum predictions of a temporal series. The resulting spectra are smoother and reduce requirements on data, but this approach may result in peak splitting, giving spurious modes. This is a concern when a higher order analysis is used, and care must be taken in choosing the length of the analysis filter. To determine if this approach should be considered in this work, a comparison with FFT is appropriate. A review of this spectral estimation approach found in Burg [38,39] follows.

The pressures constitute a series, where p_n is the nth value and the sampling period is Δt. The autocorrelation of these pressure is

$$\phi(\tau) = \lim_{T\to\infty} \frac{1}{2T+1} \sum_{n=-T}^{T} p_n p_{n+\tau} \tag{29}$$

The power spectrum of this pressure series is defined as

$$P(f) = \frac{1}{W} \sum_{\tau=-\infty}^{\infty} \phi(\tau) \cos(2\pi f \tau \Delta t) \tag{30}$$

Here, $W = \frac{1}{2\Delta t}$, and f is defined on the interval $(0, W)$. The entropy of this power spectrum is related to

$$\int_0^W \log[P(f)]\,\mathrm{d}f \tag{31}$$

The goal of this method is to determine the power spectrum that has the maximum entropy, but is constrained so that the spectrum agrees with the autocorrelation values. This constraint can be written mathematically as

$$\int_0^W P(f) \cos(2\pi f \tau \Delta t)\,\mathrm{d}f = \phi(\tau) \tag{32}$$

This maximum entropy spectrum is

$$P(f) = \frac{\frac{P_{N+1}}{W}}{|1 + \sum_{n=1}^{N} \Gamma_{n+1} e^{-i2\pi f n \Delta t}|^2} \tag{33}$$

The key component of spectral estimation is the evaluation of the autocorrelation values. Autocorrelation of this series may be estimated by Eq. (29). The problem with this estimation lies in the implicit assumption that the data before and after the limits of the series are either zero or repeat periodically as assumed by FFT. Burg [38,39] avoids this edge distortion by directly relating the autocorrelation coefficients to the power. These filter parameters values are then determined in a recursive manner beginning with a two-point autocorrelation prediction error. The filter of the pressure defined by $p_{i+1} + \Gamma_1 p_i$ has a total forward and backward squared error of

$$P_2 = \frac{1}{2(N-1)} \left[\sum_{i=1}^{N-1} (p_{i+1} + \Gamma_1 p_i)^2 + \sum_{i=1}^{N-1} (p_i + \Gamma_1 p_{i+1})^2 \right] \tag{34}$$

The minimum error is achieved when the filter parameter is

$$\Gamma_1 = -\frac{2\sum_{i=1}^{N-1} p_i p_{i+1}}{p_1^2 + 2\sum_{i=2}^{N-1} p_i^2 + p_N^2} \tag{35}$$

The next level of recursion begins with the error of a three-point filter:

$$P_3 = \frac{1}{2(N-2)} \left[\sum_{i=1}^{N-2} (x_{i+2} + \Gamma_2 x_{i+1} + \Gamma_3 x_i)^2 + \sum_{i=1}^{N-1} (x_i + \Gamma_2 x_{i+1} + \Gamma_3 x_{i+2})^2 \right] \tag{36}$$

A value of $\Gamma_2 = \Gamma_1(1 + \Gamma_3)$ is substituted to guarantee the estimate of the one-point autocorrelation agree between the two and three-point predictions. The minimization of P_3 gives the prediction parameter Γ_3. Along with the previously calculated Γ_1, Γ_2 can be calculated completing knowledge of the three-point parameters.

Table 3 Mode frequencies on the cavity floor for differing turbulence models and meshes

Data source	Mesh	Mode 2, Hz	Error, %	Mode 3, Hz	Error, %	Mode 4, Hz	Error, %
Experiment [23]	——	353 ± 12	——	594 ± 12	——	838 ± 12	——
LES [8]	M1	462	30.9	625	5.2	873	7.1
KES	1R	337	−4.5	675	13.6	1012	24.5
LES [8]	M3	362	2.5	594	0.0	813	3.1
GT-HRLES	2R	379	7.4	611	2.9	846	4.0
KES	2R	377	6.8	628	5.7	844	3.8

In a similarly recursive manner the parameters of the filter up to the desired order of prediction are determined. This procedure is continued until the desired number of filter points (the order) of the system is reached. These parameters are substituted into Eq. (33) to obtain the estimation of the power spectrum:

$$p(t) = \sin(2\pi \cdot 1 \cdot t) + \sin(2\pi \cdot 2 \cdot t) + \sin(2\pi \cdot 3 \cdot t) + \sin(2\pi \cdot 4 \cdot t) \quad (37)$$

A comparison of the results of the cavity simulation with 0.5 s of GT-HRLES data analyzed using Burg's [38,39] methods with varying orders (Fig. 5) demonstrates sensitivity of the method to the chosen order. At the lowest order of 500, the spectrum has a high degree of smoothing with variation in the data reduced, whereas at the highest order of 2000 the data show spurious peaks and even a triple peak at the 594 Hz peak. An order of 1000 provides a balance between reproducing variability in the data without additional peak splitting. As previously outline, sensitivity to order demands careful consideration to avoid spurious peaks.

The results of Burg's [38,39] spectral estimation using an order of 1000 as compared with traditional FFT (Fig. 6) have much smoother sound pressure levels and lower sound pressure levels at the higher frequencies. With Burg's [38,39] method a large order is needed to allow the complex spectrum to be reconstructed, resulting in the attenuation of higher frequencies due to the dependence of the prediction parameter on the longer period oscillations. The predicted mode frequencies (Table 4) fall within the error bounds of the experiment and analysis. The similar predictions for the acoustics in terms of the mode frequencies and amplitudes (Tables 4 and 5) might lead to the conclusion that Burg's [38,39] method is desirable, due to its smoother frequency spectrum, however, the sensitivity to the order creates a source of uncertainty in the approach. Therefore, the traditional FFT analysis is applied for the remainder of the analysis within this paper.

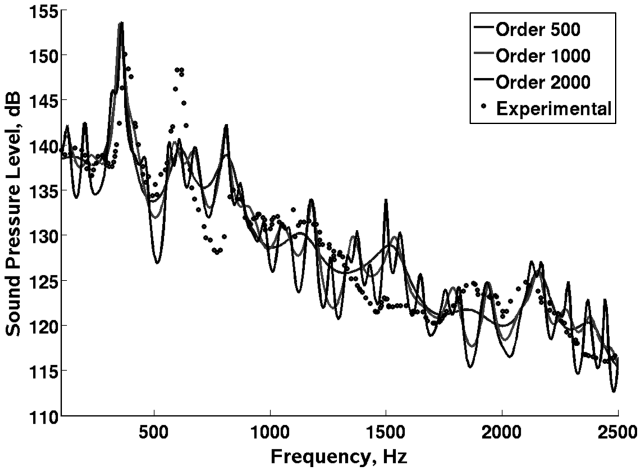

Fig. 5 Sound pressure levels at the cavity floor center using Burg's [38,39] method with varying orders.

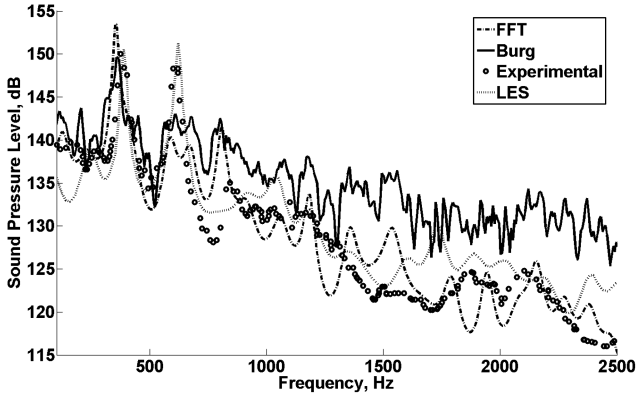

Fig. 6 Sound pressure levels at the cavity floor center using Burg's [38,39] method and FFT.

Table 4 Peak mode frequency error for differing spectral methods

Mode	FFT error, %	Burg [38,39] error, %
2	−3.9	−4.6
3	−0.4	−3.2
4	−4.6	−4.0

Table 5 Peak mode amplitude error for differing spectral methods

Mode	FFT error, %	Burg [38,39] error, %
2	−0.4	2.2
3	−3.7	−5.4
4	5.4	4.6

D. Flowfield Evaluation

In prior computational analyses, it was noted [11] that the RANS-based methods were able to capture the large flowfield features but dissipated the vorticity over time. This behavior is examined here by comparing the flowfields from each of the different turbulence simulations at two different simulation times. In Fig. 7, the flowfield vorticity at 8 ms is seen on the left, while the flowfield 2 ms later is shown on the right. All methods capture the separation after the upstream corner of the cavity, leading to a recirculation region immediately behind the backward facing step and vortex shedding which reaches the downstream corner. Vorticity at the downstream corner travels either over the corner or towards the bottom of the cavity via the rear wall. The feedback loop of vorticity is reproduced in each set of data, however, significant differences in the overall character of the flowfields for each simulation.

The traditional RANS flowfield defines several vortical structures in the shear layer that have developed from the forward edge of the cavity. As time progresses, the vortices, as noted by vortex A, move downstream and impinge on the aft cavity wall. Vortices resulting from this wall impingement travel forward toward the front of the cavity, as illustrated by vortex B. One issue in this flowfield is the high degree of dissipation. Although the flow separates at the upstream corner, separation is not apparent at the downstream corner and vorticity within the cavity is relatively weak. This field differs significantly from the DES-SST simulation, which captures a large amount of vorticity. This fact is attributed to the subgrid-scale modeling allowing resolution of eddies that are modeled in traditional RANS. In the DES-SST vorticity flowfield in Fig. 7b, vortex A travels downstream impinging on the corner, while vortices B and C are traveling upstream across the cavity floor. Although much more vorticity is captured by the DES-SST method, the GT-HRLES approach predicts stronger vortex cores. Moreover, the effect of the cavity extends further into the far field than the DES-SST results with more shed vorticity. Separation on the downstream corner is stronger for the GT-HRLES technique than DES-SST work. The KES simulation does not capture as complex of a flowfield when compared with the hybrid RANS-LES data, but it captures more of the vortical structures than traditional RANS. The vortex cores are weaker for the KES data than in the GT-HRLES case, but stronger than those acquired via the traditional RANS and DES-SST models. The shear layer downstream and cavity flow upstream vortex motion are clearly seen in vortices labeled A, B and C, D, respectively. The vorticity captured by the DES-SST and GT-HRLES simulations missing in the KES data may be attributed to the direct transport of turbulent dissipation in conjunction with subgrid-scale modeling in contrast to the KES method which scales the $(kl)^{sgs}$ term. Dissipation throughout the flowfield is better preserved using the DES-SST and

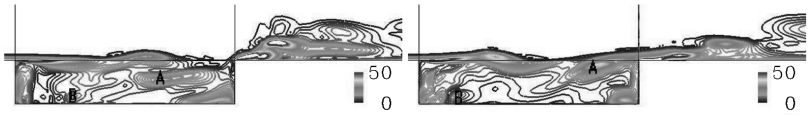

a) Menter $k - \omega$ SST simulation

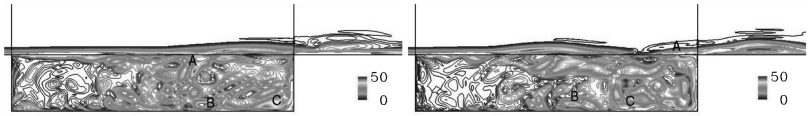

b) DES-SST simulation

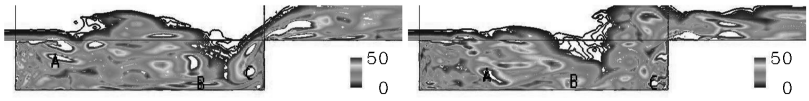

c) GT-HRLES simulation

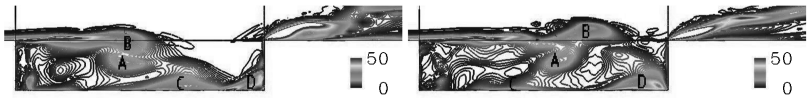

d) KES simulation

Fig. 7 Vorticity within the cavity for the different turbulence methods. The flowfield at 8 ms is on the left and at 10 ms on the right.

GT-HRLES methods, resulting in the flowfield having many distinct vortices.

E. Flow Development

Initial investigation of subsidence of the initial flow transients of the integrated load coefficients for the simulations is presented for grid 2R. The cavity floor pressure was integrated over the cavity floor and normalized to coefficient form:

$$C_N = F_N \Big/ \frac{1}{2}\rho_\infty U_\infty^2 S_{\text{ref}} \tag{38}$$

As the pressure changes across the floor, the integrated normal force will provide a measure of the time at which the initial transients in the flow have died down. The coefficient of normal force is illustrated for each of the turbulence approaches in Fig. 8. In each case the coefficient of normal force shows some degree of oscillation

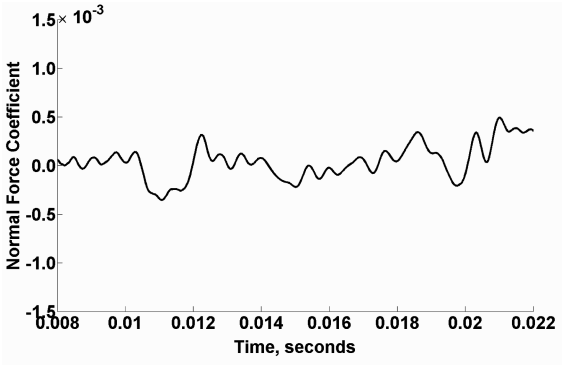

a) Menter $k - \omega$ SST simulation

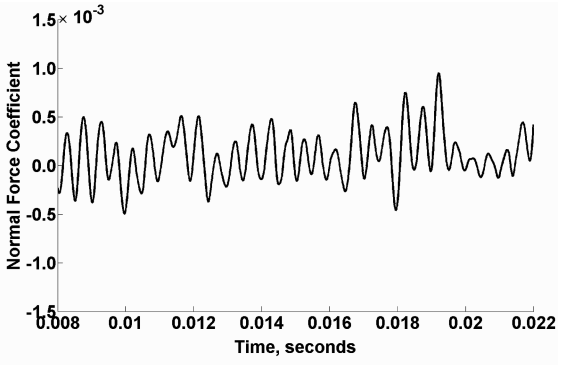

b) DES-SST simulation

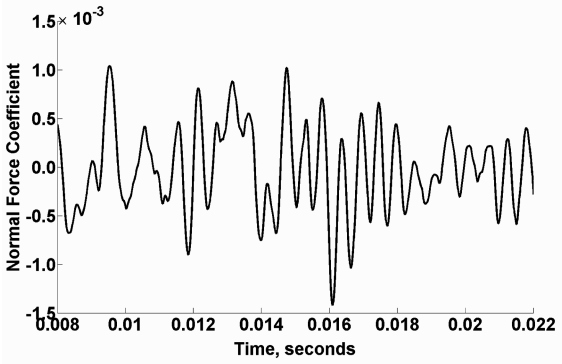

c) GT-HRLES simulation

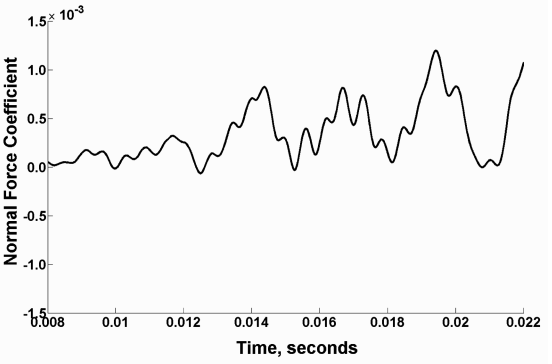

d) KES simulation

Fig. 8 Periodic development of normal force on the cavity floor.

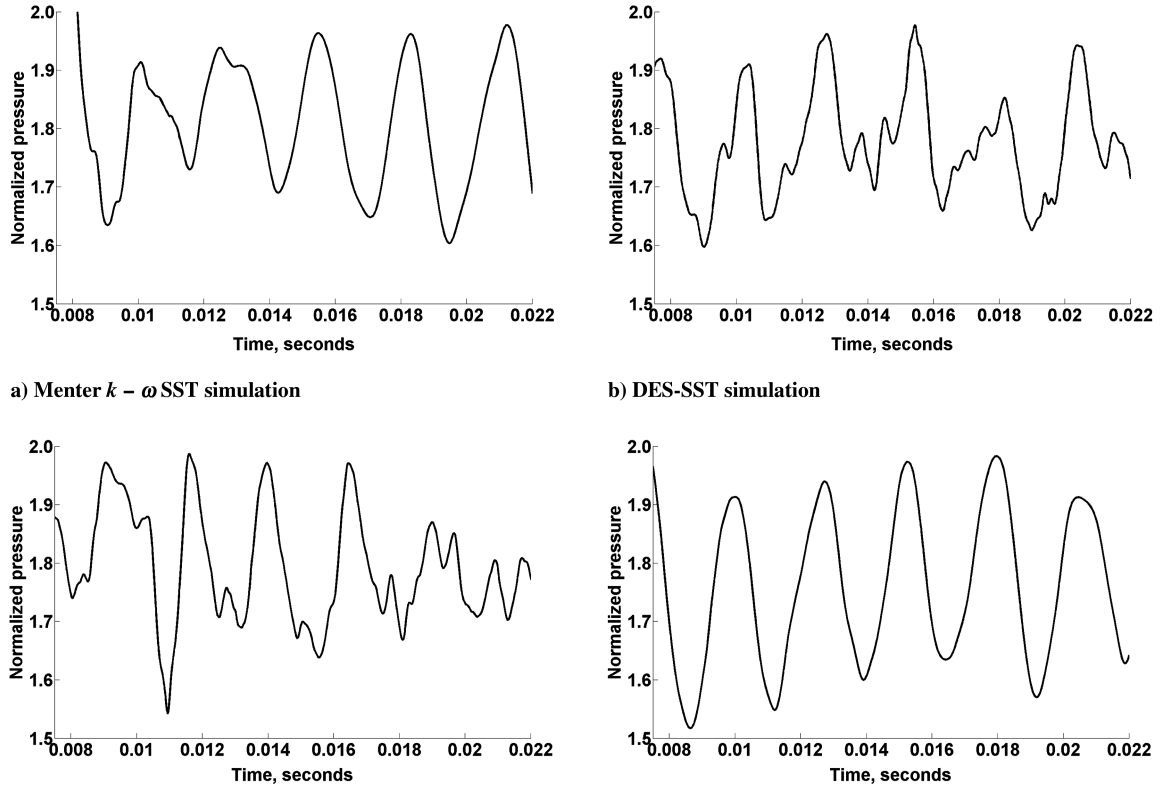

a) Menter $k-\omega$ SST simulation

b) DES-SST simulation

c) GT-HRLES simulation

d) KES simulation

Fig. 9 Pressure history on the cavity floor.

resulting from the unsteady vortex structure within the cavity. The k-ω SST results have the weakest oscillations, as expected from the highly dissipative model. Variations for the DES-SST data are greater than for traditional RANS, but the GT-HRLES data demonstrate the largest multiscale oscillations. The LES-VLES approach captures stronger oscillations than traditional RANS, but differs from DES-SST and GT-HRLES as it has differing transported properties.

The pressure histories at the cavity floor midpoint in Fig. 9 indicate a strong simple harmonic content over much of the time period, indicative of the influence of the vortical feedback loop, although the magnitude and phase of the pressure varies for each of the three turbulence approaches. The DES-SST and GT-HRLES pressures also contain higher harmonics not present in the other two methods resulting from the higher vortical activity observed in Fig. 7.

The pressure histories were then analyzed by taking the frequency transform to obtain acoustic and frequency characteristics. Data analysis begins after the starting transients have exited the computational domain and periodicity in the solution is observed. Three different analysis intervals of 5.81, 11.70, and 17.36 residence periods that use subsequently more data from the pressure history trace were examined to ascertain the time required for the initial flow transients to subside. These intervals correspond to an integer-based number of pressure cycles from the pressure data in order to avoid biasing of the data.

The mean pressure on cavity floor (Table 6) provides a starting point in determining if the initial transients have died out, which is defined as when the mean pressure changes were less than 1.5% between analysis intervals. The mean pressure for the k-ω SST simulation final averaged value obtained is 2.9% higher than the mean pressure from the GT-HRLES simulation and 3.8% higher than the KES simulation predictions. The DES-SST results fall between traditional RANS and the higher fidelity methods. This discrepancy between the RANS and hybrid results is explained by the dissipative nature of the RANS approach. The k-ω SST, DES-SST, and KES simulations have pressure changing less than 1.5% by the end of the analysis interval. For the GT-HRLES case, the simulation time was extended for an addition 8 residence periods to ensure the flow was fully developed. A change of less than 0.1% was computed when compared with the 17.36 residence period case confirming the fully developed cavity flow.

In addition to static pressure analysis, dependency of the solution on the interval of data analysis is necessary through the acoustic response of the flow. This analysis provides evidence that adequate data is contained to obtain a refined frequency spectrum. The frequency analysis of the pressure history data in Fig. 9 presents frequency characteristics in the form of the sound pressure levels in Fig. 10. Each of the analysis intervals is indicated by a different line style. As expected, the results from the shortest (5) residence period analysis do not correlate well with the experimental data, as enough time is not included to resolve the harmonics. The traditional RANS data containing the longest time interval capture the frequencies of modes 2, 3, and 4, but do not accurately predict their amplitudes. The hybrid simulations indicate lower amplitude at very low frequencies, which are not observed in the RANS case, where the amplitude

Table 6 Mean pressures at the cavity floor center for OVERFLOW simulations

Case	Pressure, 5.81 res, kPa	Pressure, 11.70 res, kPa	Pressure, 17.36 res, kPa
k-ω SST	163.0	160.6	159.4
DES-SST	160.3	156.8	156.9
GT-HRLES	158.9	156.9	154.9
KES	151.8	152.8	153.5

Table 7 Predicted cavity modal frequencies for different turbulence methods and analysis intervals

Interval, res	Mode 2, Hz	Error, %	Mode 3, Hz	Error, %	Mode 4, Hz	Error, %
			k-ω SST			
5.81	338	−4.4	632	6.4	800	−1.6
11.70	317	−10.3	591	−0.6	800	−1.6
17.36	317	−10.3	614	3.2	800	−1.6
			DES-SST			
5.81	250	−29.3	——	——	715	−12.1
11.70	325	−7.8	615	3.6	818	0.6
17.36	332	−5.9	552	−7.1	778	−4.3
			GT-HRLES			
5.81	337	−4.5	590	−0.7	843	3.7
11.70	379	7.4	590	−0.7	843	3.7
17.36	379	7.4	611	2.9	843	3.7
			KES			
5.81	506	39.6	——	——	1012	20.7
11.70	422	16.5	759	19.7	1181	40.9
17.36	338	−7.8	549	−5.4	929	10.8
			Rossiter [37]			
——	357	1.3	566	4.7	775	4.7
			LES simulations [8] *(mesh 3)*			
——	362	2.5	594	0.0	838	3.1
			Experiment [23]			
——	353 ± 12	——	594 ± 12	——	813 ± 12	——

continues to increase as the frequency drops. For the KES simulation, the first two modes merge into one single mode for the shortest analysis interval, but become distinct as the analysis interval is increased. As the amount of pressure data increases with longer analysis intervals the harmonic content becomes more pronounced. Tables 7 and 8 for the frequency locations and amplitudes, respectively, indicate convergence to values that agree the with experimental results to within the error bounds. Experimental data, analytical predictions from Rossiter, and LES results are also shown for comparison. The longest analysis time period yields errors of less than about 10% of the mean (within the 12% error bound) for the harmonic frequencies and amplitudes. The RANS method performs as well as the hybrid methods in determining the frequencies and amplitudes of the harmonics though the high mean pressures and sound levels at low frequencies provide evidence of its predictive limitations. The DES-SST and GT-HRLES methods predict harmonic modes are more distinct than those predicted by the KES approach, as one would expect from the differences in the vorticity observed in Fig. 7, but the DES-SST predictions have larger relative errors in the peak location and amplitudes than the GT-HRLES predictions. The LES simulations [8,23] outperform all other methods in overall terms of relative error, as expected.

F. Time Step Analysis

A longer analysis interval with a simulation time of 0.5 s is considered. The original physical time step applied in this effort was computed to be 3.62×10^{-6} to ensure that the temporal integration was appropriate to accurately capture up to 500 Hz frequencies. This resulted in a simulation time of approximately 0.07 s, which is significantly less than the minimum necessary simulation time of 0.5 s cited by Allen and Mendonca [24]. However, the time step of 3.62×10^{-6} s was also significantly smaller than the time step of $2. \times 10^{-5}$ s used in Allen's simulations. An additional simulation using the GT-HRLES turbulence approach was computed with this larger time step of $2. \times 10^{-5}$ to the 0.5 s simulation time to examine the influence of these quantities on the aeroacoustic predictions. This larger time step is used to gather a much longer time sample, but it is important to justify both the small and large time steps. For the small time step consideration is taken towards the longest Rossiter mode [37] of the cavity, which occurs at 148 Hz. Despite the short simulation time, the small time step simulations are able to capture the frequencies of the higher harmonics. Justification of the analysis interval stems from consideration of the Rossiter mode interactions. Experiments [42] have confirmed that Rossiter modes interact and lead to the addition smaller peaks in the frequency spectrum, rather than alteration of the dominant modes. The result is that time

Table 8 Predicted cavity modal amplitudes for different turbulence methods and analysis intervals

Interval, res	Mode 2, dB	Error, %	Mode 3, dB	Error, %	Mode 4, dB	Error, %
			k-ω SST			
5.81	151	0.6	149	0.7	147	8.6
11.70	149	−0.5	147	−0.9	143	5.8
17.36	148	−1.7	144	−2.6	141	4.6
			DES-SST			
5.81	150	0.5	——	——	147	8.8
11.70	151	0.9	146	−1.4	145	7.3
17.36	152	1.4	146	−1.5	143	6.1
			GT-HRLES			
5.81	150	0.0	148	−0.3	144	6.5
11.70	150	0.1	145	−1.9	143	6.0
17.36	151	0.3	145	−1.7	142	5.4
			KES			
5.81	153	2.1	——	——	149	10.4
11.70	155	3.3	147	−0.7	145	7.4
17.36	153	2.1	147	−0.7	144	7.0
			Experiment [23]			
——	150	——	148	——	135	——

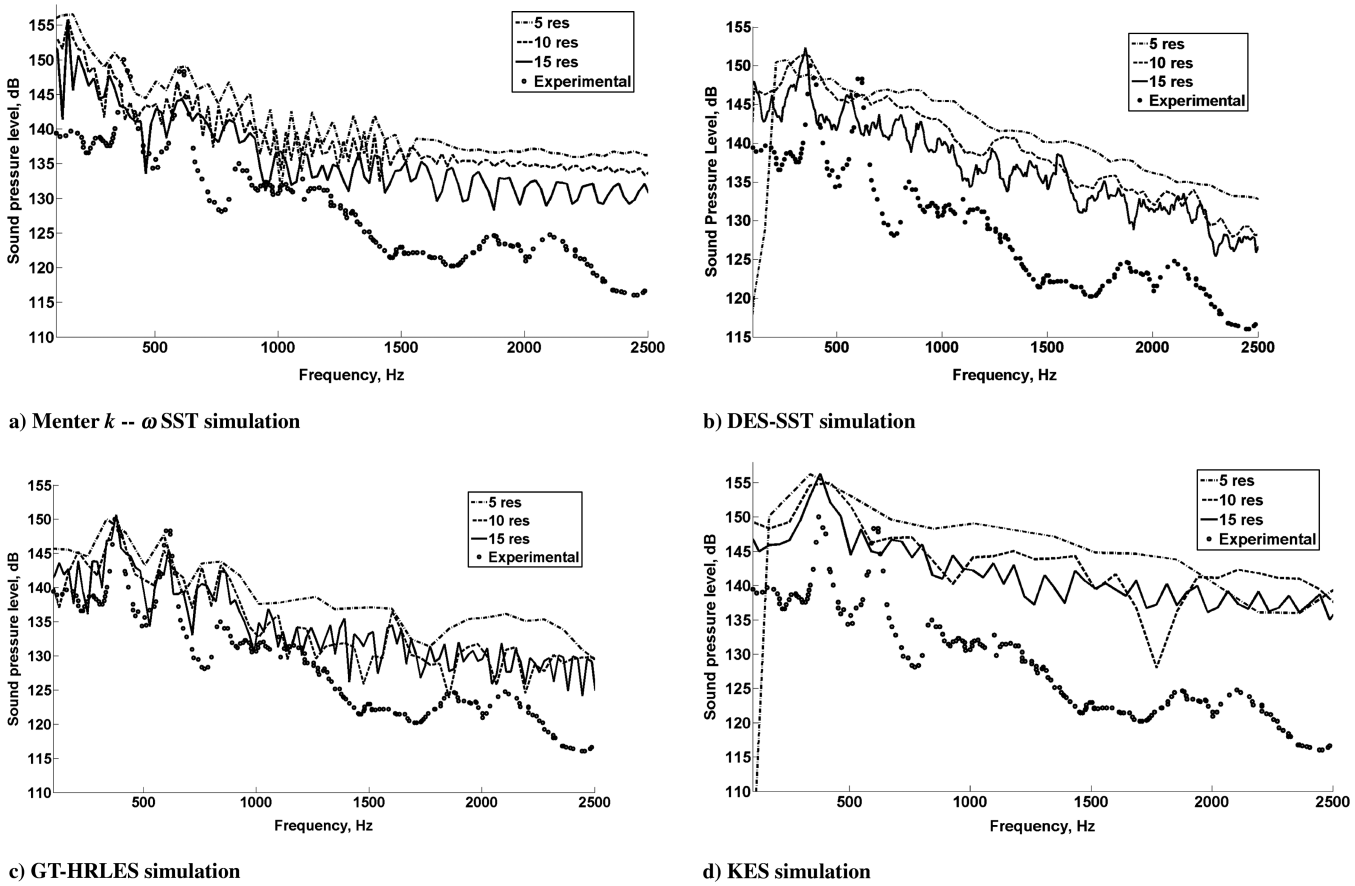

a) Menter k -- ω SST simulation

b) DES-SST simulation

c) GT-HRLES simulation

d) KES simulation

Fig. 10 Sound pressure levels for cavity pressure data.

intervals that are not long enough to reproduce the lowest frequencies may still be used to investigate the higher frequency dominant modes. For the large time step the long simulation time of 0.5 s is adequate to resolve the longer modes, but consideration is placed on resolution of the highest frequencies. The third Rossiter mode of the cavity occurs at 566 Hz giving 11,320 samples per oscillation cycle for this large time step, which is more than adequate resolution of the signal.

First, an analysis at the end of 0.07 s simulation time with the larger time step was examined, excluding the initial transient. This was equivalent to the 17.36 residence time studied for the smaller time step. The larger time step was not able to adequately resolve some of the higher mode frequencies during this short simulation period. The frequency of the first mode was predicted within the experimental error bounds, but the prediction errors of the higher modal frequencies grew significantly larger with increasing mode number. The first three modal sound pressure levels were predicted within 3% and did not vary significantly from the predictions at this simulation time by the smaller time step. The increasing error in the modal frequency location was not unexpected as the larger time step does not have as high a sampling rate as the smaller time step, and as the frequency is increased fewer samples per cycle are gathered leading to less accuracy. Additionally, there are 5 times fewer samples for the larger time step simulations during the simulation time.

The residence period analysis used to evaluate convergence indicated that the larger time step required the entire simulation interval (minus the transient portion of the simulation) to converge on the first four modal characteristics. The sound pressure levels for the different GT-HRLES simulations (Fig. 11) indicate that overall the predictions for the smaller time step and simulation interval ($\Delta t = 3.62 \times 10^{-6}$, $t = 0.07$ s) is overall fairly comparable to those from the larger time step and simulation interval ($\Delta t = 2. \times 10^{-5}$, $t = 0.5$ s). The larger time step/interval combination captures the SPL levels within 2–3 dB of experiment below 100 Hz, while the smaller time step/interval combination can vary as much as 5 dB. The anomalous SPL increase that was previously observed between 700–1000 Hz is still present, indicating that the sampling time is not the source of this discrepancy. At frequencies above 1000 Hz, the overall trend of the larger time step/interval combination is to reduce the broadband SPL levels, moving them closer to the experiment. It should be noted that this study was not designed originally to capture these frequencies, but with a more appropriate grid, this observation can prove to be helpful.

The modal frequencies (Table 9) are more accurately reproduced by the larger time step/longer analysis interval, falling within the error bounds of the experiment with the exception of mode 4. Conversely, the peak SPL (Table 10) is not significantly influenced by either a longer time interval or the larger time step. The smaller time step more accurately captures the SPLs compared with experiment, however, the overall differences between the values is less than 2% for the fourth mode and less for the lower modes.

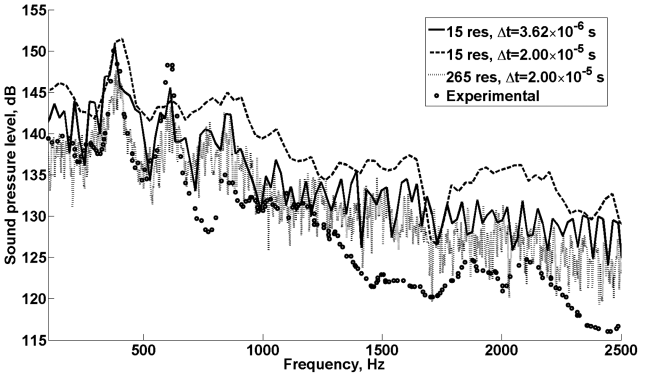

Fig. 11 Influence of run time on sound pressure levels for the GT-HRLES turbulence method.

Table 9 GT-HRLES predicted cavity modal frequencies for different time steps and analysis intervals

Source	Interval, res	Mode 2, Hz	Error, %	Mode 3, Hz	Error, %	Mode 4, Hz	Error, %
$\Delta t = 2.00 \times 10^{-5}$ s	17.36	388	10.0	615	3.5	847.7	4.3
$\Delta t = 2.00 \times 10^{-5}$ s	265	354	0.3	596	0.3	837	3.0
$\Delta t = 3.62 \times 10^{-6}$ s	17.36	385	9.0	614	3.4	838	3.1
Experiment [23]	——	353 ± 12	——	594 ± 12	——	813 ± 12	——

Table 10 GT-HRLES predicted cavity modal SPL for different time steps and analysis intervals

Source	Interval, res	Mode 2, dB	Error, %	Mode 3, dB	Error, %	Mode 4, dB	Error, %
$\Delta t = 2.00 \times 10^{-5}$ s	17.36	151	0.9	144	−3.0	145	7.3
$\Delta t = 2.00 \times 10^{-5}$ s	265	149	−0.6	145	−2.1	144	6.7
$\Delta t = 3.62 \times 10^{-6}$ s	17.36	151	0.3	145	−1.7	142	5.4
Experiment [23]	——	150	——	148	——	135	——

G. Grid Node Distribution

If hybrid turbulence methodology is applied using a RANS-like approach with the goal of improving flow reproduction, solution dependency on grid node distribution should be addressed. The previous results obtained using the RANS-like grid with larger spacing across the center of the cavity are compared with results using a grid with more node clustering in the center of the cavity that could be employed with an LES code (Fig. 12). The only difference between the two simulations shall be the grid node distribution. With both grids the GT-HRLES approach is used with the same discretization and integration parameters. Pressure is taken again at the same cavity floor location and estimation of the frequency spectrum is carried out with FFT. The results of the spectral analysis

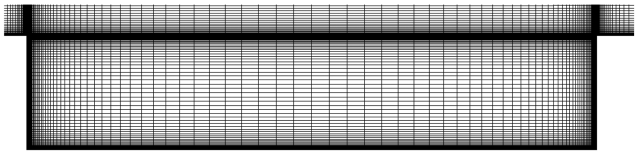

a) RANS-like grid node distribution

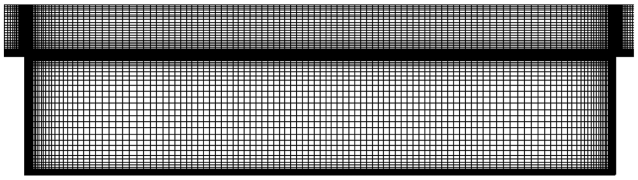

b) LES-like grid node distribution

Fig. 12 Differing node distributions for grid dependency analysis.

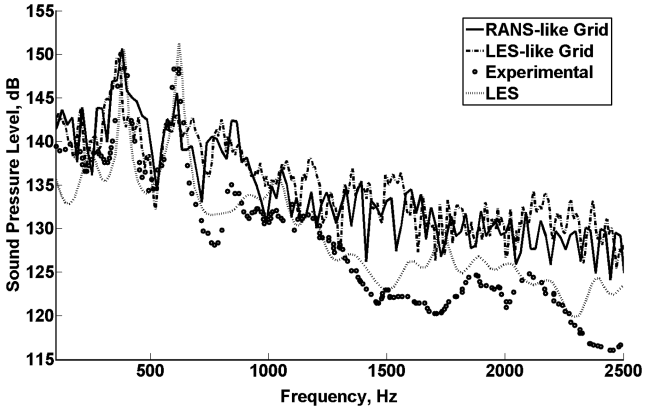

Fig. 13 Sound pressure levels at the cavity floor center using differing node distributions.

Table 11 Peak mode frequency error for differing node distributions

Mode	RANS-like error, %	LES-like error, %
2	2.6	−3.9
3	0.2	−0.4
4	1.8	−4.6

Table 12 Peak mode amplitude error for differing node distributions

Mode	RANS-like error, %	LES-like error, %
2	0.4	−0.4
3	−1.9	−3.7
4	5.4	5.4

(Fig. 13) give minimal qualitative difference between the differing node distributions. Quantitatively, a comparison of the mode predictions (Tables 11 and 12) provides evidence that the frequencies predicted by each method fall within the analysis error of each other, providing evidence of the validity of the RANS-like grid approach. All mode frequency predictions fall within the error bounds of the experiment with the exception of mode 4 for the LES-like grid results.

H. Method Evaluation

As a final evaluation, the 0.5 s period DES-SST and GT-HRLES results are compared with the results obtained by LES [8] and experiments by Henshaw [23]. The sound pressure levels for these simulations (Fig. 14) are presented up to frequencies of 2500 Hz (Fig. 15). The DES-SST method predicts additional modes between 100–400 Hz, which are not present in experiment. The GT-HRLES turbulence method simulation captures overall more accurate SPL characteristics below 700 Hz than the DES-SST approach and is comparable to the LES predictions. The major characteristics of the mode at 350 Hz are captured by the LES and GT-HRLES simulations. The DES-SST approach captures this peak, but the frequency is shifted. The third mode is best captured by the LES method, with the GT-HRLES method providing the next best predictions. The DES-SST result for the third mode is the most inaccurate correlation. As discussed previously, the grids for the DES-SST GT-HRLES simulations were not optimized for higher frequency content and contained some aspect ratios that may result in poorer resolution of the acoustics above 700 Hz.

With respect to the captured modal frequencies (Table 13), GT-HRLES computation at the longer simulation time/larger time step combination predicts the frequencies with accuracy comparable to

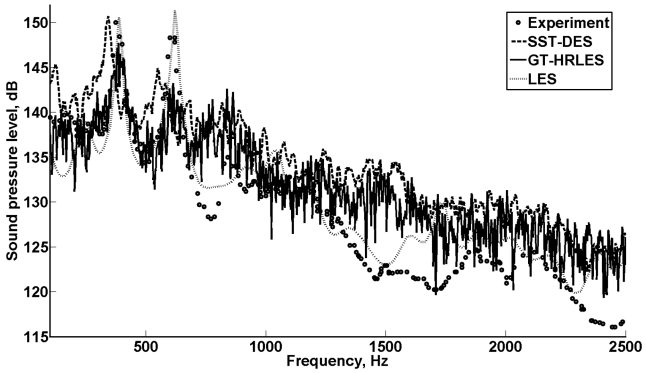

Fig. 14 Sound pressure levels at the cavity floor center for different turbulence methods [8,23].

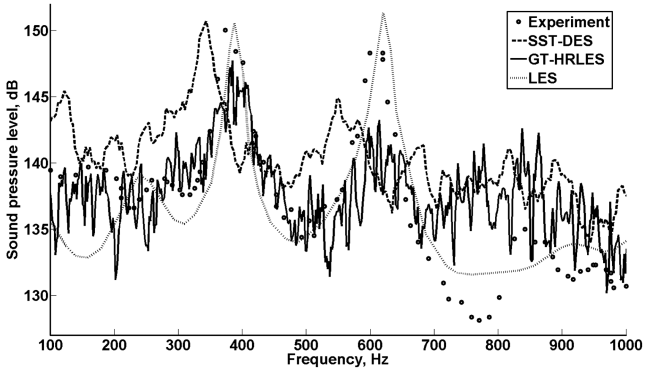

Fig. 15 Sound pressure levels at the cavity floor center for different turbulence methods [8,23].

the LES simulation for the second and third modes, and is comparable to the other hybrid methods for mode four. For the modal peak sound pressure levels (Table 14), the GT-HRLES and DES-SST predictions for modes two and three are comparable to LES, but mode four DES-SST and GT-HRLES levels are not as accurate as the LES results. Limited computer resources prevented examination of a longer time interval to determine if this could have lowered the higher mode amplitudes. As expected, the LES method has the best performance overall. The GT-HRLES approach is the next most accurate after LES.

Some final consideration of cost is appropriate. The hybrid turbulence techniques employed in this study aim to improve predictions of cavity flows without drastically increasing the cost of the simulations. The DES-SST, GT-HRLES, and KES techniques result in an increase in cost relative to the traditional RANS approach of 2.1, 16, and 0.9%, respectively. No timing information was available for the comparable LES study, so quantitative comparisons are not possible, but qualitative assessments may be made. If timing data from recent LES simulations by Tucker et al. [43] employing structured grids in an LES framework are considered, full LES simulation with appropriate temporal parameters would increase the cost by 2 orders of magnitude. The advanced turbulence methods outlined in this study provide a much higher turnover rate for modestly decreased accuracy.

V. Conclusions

A series of analyses using different turbulence simulations, including RANS Menter $k\omega$ SST, two hybrid RANS/LES methods known as DES-SST and GT-HRLES, and an LES-VLES technique known as KES, have been evaluated in a legacy RANS code, OVERFLOW, for a 5:1:1 cavity in a transonic freestream ($M_\infty = 0.85$). Characteristics of the simulations using time step size and simulation length have been examined. From these simulations, several conclusions can be reached:

1) All four turbulence approaches predict the large feedback vortical structures within the cavity, but only the DES-SST and GT-HRLES methods capture additional flowfield complexity, which may be due to the explicit transport of turbulent dissipation with subgrid-scale modeling.

2) Higher harmonics are apparent in the DES-SST and GT-HRLES simulations, which are not as apparent in the traditional RANS and KES approaches resulting from the large amount of complex vorticity apparent in the flowfield.

3) Verification of subsidence of initial transients and onset of periodicity of the simulations can be determined via the mean of the integrated pressures on the cavity floor with increasing analysis interval.

4) The RANS and KES models over-predict the overall sound pressure levels. The DES-SST method predicts lower sound pressure levels, but the GT-HRLES predictions are the most accurate when correlated with experimental measurements and LES results.

5) Comparisons of 0.5 s simulation interval frequency predictions for DES-SST and GT-HRLES methods demonstrates reproduction of the second and third harmonics much more accurately for GT-HRLES. The fourth harmonic is captured with a similar level of accuracy between the two methods. All predictions fall within error bounds of the analysis. The GT-HRLES modal frequencies are sensitive to time step size and simulation length. This confirms the need for a 0.5 s simulation interval by Allen and Mendonca [24].

6) The GT-HRLES predictions of the peak modal sound pressure levels for frequencies below 1000 Hz are less sensitive to the time step size and simulation length than modal frequency locations,

Table 13 Comparison of cavity modal frequencies

Method	Mode 2, Hz	Error, %	Mode 3, Hz	Error, %	Mode 4, Hz	Error, %
DES-SST	323	−8.4	538	−9.4	790	−2.9
GT-HRLES	354	0.3	596	0.3	837	3.0
LES [8], mesh 3	362	2.5	594	0.0	813	0.0
Experiment [23]	353 ± 12	——	594 ± 12	——	813 ± 12	——

Table 14 Comparison of cavity modal peak sound pressure levels

Method	Mode 2, dB	Error, %	Mode 3, dB	Error, %	Mode 4, dB	Error, %
DES-SST	151	0.4	144	−2.4	141	4.5
GT-HRLES	149	−0.6	145	−2.1	144	6.7
LES [a][8] (mesh 3)	150	0.3	151	2.2	134	−1.0
Experiment [23]	150	——	148	——	135	——

[a]These data were not explicitly given by Levasseur et al. [8]. These quantities have been determined by digitization of the SPL data presented in Fig. 14.

negating the recommendation of a 0.5 s simulation interval by Allen and Mendonca [24].

7) The DES-SST and GT-HRLES predictions have similar performance for the 0.5 s analysis interval in terms of sound pressure level predictions. These predictions are comparable to previously published LES predictions for frequencies below 600 Hz for which this study was designed.

8) The GT-HRLES approach was able to predict SPL for the peak frequencies below 400 Hz within 1 dB and below 600 Hz within about 2 dB. Above 600 Hz, the SPL predictions were within 10 dB, indicating the need for a grid with reduced aspect ratios and stretching below 15%, which was used in the present study.

References

[1] Efimtsov, B., Golubev, A., and Anderson, A., "Pressure Fluctuations in and Around a Flow-Grazed Cavity at Transonic Velocities," 13th AIAA/CEAS Aeroacoustics Conference (28th AIAA Aeroacoustics Conference), AIAA Paper 2007-3414, Rome, 2007.

[2] Driver, D. M., Seegmiller, H. L., and Marvin, J. G., "Time-Dependent Behavior of a Reattaching Shear Layer," *AIAA Journal*, Vol. 25, No. 7, 1987, pp. 914–919. doi:10.2514/3.9722

[3] Ritchie, S., Lawson, N., and Knowles, K., "An Experimental and Numerical Investigation of an Open Transonic Cavity," 21st Applied Aerodynamics Conference, AIAA Paper 2003-4221, Orlando, FL, 2003.

[4] Chung, K., "Transonic Cavity-Convex Corner Interaction," *Journal of Aircraft*, Vol. 40, No. 6, 2003, pp. 1131–1136. doi:10.2514/2.7201

[5] Komerath, K., Ahuja, K., and Chambers, F., "Prediction and Measurement of Flows Over Cavities: A Survey," AIAA 25th Aerospace Sciences Meeting, AIAA Paper 0087-0166, Reno, NV, 1987.

[6] Shrinivasan, S., and Baysal, O., "Navier–Stokes Calculations of Transonic Flows Past Cavities," *Journal of Fluids Engineering*, Vol. 113, No. 3, 1991, pp. 368–376. doi:10.1115/1.2909506

[7] Zhang, X., "Compressible Cavity Flow Oscillation due to Shear Layer Instabilities and Pressure Feedback," *AIAA Journal*, Vol. 33, No. 8, 1995, pp. 1404–1411. doi:10.2514/3.12845

[8] Levasseur, V., Sagaut, P., Mallet, M., and Chalot, F., "Unstructured Large Eddy Simulation of the Passive Control of the Flow in a Weapon Bay," *Journal of Fluids and Structures*, Vol. 24, No. 8, 2008, pp. 1204–1215. doi:10.1016/j.jfluidstructs.2008.06.016

[9] Thornber, B., and Drikakis, D., "Implicit Large-Eddy Simulation of a Deep Cavity Using High-Resolution Methods," *AIAA Journal*, Vol. 46, No. 10, 2008, pp. 2634–2645. doi:10.2514/1.36856

[10] Lawson, S., and Barakos, G., "Assessment of Passive Flow Control for Transonic Cavity Flow Using Detached-Eddy Simulation," *Journal of Aircraft*, Vol. 46, No. 3, 2009, pp. 1009–1029. doi:10.2514/1.39894

[11] Tam, C., Orkwis, P., and Disimile, P., "Comparison of Baldwin–Lomax Turbulence Models for Two-Dimensional Open Cavity Computations," *AIAA Journal*, Vol. 34, No. 3, 1996, pp. 629–631. doi:10.2514/3.60019

[12] Kim, H., Aradag, S., and Knight, D., "Two and Three Dimensional Simulations of Supersonic Cavity Flow," 12th AIAA/CEAS Aeroacoustics Conference (27th AIAA Aeroacoustics Conference), AIAA Paper 2006-2431, Cambridge, MA, 2006.

[13] Brès, G. A., and Colonius, T., "Three-Dimensional Instabilities in Compressible Flow Over Open Cavities," *Journal of Fluid Mechanics*, Vol. 599, March 2008, pp. 309–339.

[14] Premnath, K. N., and Pattison, M. J., "Large-Eddy Simulation of Self-Sustained Flow Instabilities in Cavities Using the Lattice-Boltzmann Method," *AIAA Journal*, Vol. 47, No. 1, 2009, pp. 229–243. doi:10.2514/1.38278

[15] Mincu, D., Mary, I., Manoha, E., Larchevêque, L., and Redonnet, S., "Numerical Simulations of the Sound Generation by Flow Over Surface Mounted Cylindrical Cavities Including Wind Tunnel Installation Effects," 15th AIAA/CEAS Aeroacoustics Conference, AIAA Paper 2009-3314, Miami, FL, 2009.

[16] Handa, T., and Masuda, M., "On the Jump in the Frequency of Acoustic Oscillations in Supersonic Flows Over Rectangular Cavity," *Physics of Fluids*, Vol. 21, No. 2, 2009, pp. 026102–026108. doi:10.1063/1.3081560

[17] Syed, S., and Hoffmann, K., "Numerical Investigation of 3-D Open Cavity with and Without Cover Plates," 47th AIAA Aerospace Sciences Meeting Including The New Horizons Forum and Aerospace Exposition, AIAA Paper 2009-0551, Orlando, FL, 2009.

[18] Mahmoudnejad, N., and Hoffmann, K., "Numerical Investigation of Unsteady Turbulent Flows over Cavities," 27th AIAA Applied Aerodynamics Conference, AIAA Paper 2009-3503, San Antonio, TX, 2009.

[19] Basu, D., Hamed, A., and Das, K., "DES and Hybrid RANS/LES Models for Unsteady Separated Turbulent Flow Predictions," 43rd AIAA Aerospace Sciences Meeting and Exhibit, AIAA Paper 2005-0503, Reno, NV, 2005.

[20] Li, Z., and Hamed, A., "Effect of Sidewall Boundary Conditions on Unsteady High Speed Cavity Flow and Acoustics," *Computers and Fluids*, Vol. 37, No. 5, 2008, pp. 584–592. doi:10.1016/j.compfluid.2007.07.012

[21] Spalart, P., Deck, S., Shur, M., Squires, K., Strelets, M., and Travin, A., "A New Version of Detached-Eddy Simulation, Resistant to Ambiguous Grid Densities," *Theoretical and Computational Fluid Dynamics*, Vol. 20, No. 3, 2006, pp. 181–195. doi:10.1007/s00162-006-0015-0

[22] Spalart, P., "Detached-Eddy Simulation," *Annual Review of Fluid Mechanics*, Vol. 41, Jan. 2009, pp. 181–202. doi:10.1146/annurev.fluid.010908.165130

[23] Henshaw, M., "Verification and Validation Data for Computation Unsteady Aerodynamics: M219 Cavity Case," NATO Research and Technology Org. RTO-TR-26, Oct. 2000.

[24] Allen, R., and Mendonca, F., "DES Validations of Cavity Acoustics over the Subsonic to Supersonic Range," 10th AIAA/CEAS Aeroacoustics Conference, AIAA Paper 2004-2862, Manchester, England, U.K., 2004.

[25] Buning, P., Parks, S., Cham, W., and Renze, K., "Application of the Chimera Overlapped Grid Scheme to Simulation of Space Shuttle Ascent Flows," *Proceedings of the 4th International Symposium on Computational Fluid Dynamics*, Vol. 1, 1991, pp. 132–137.

[26] Shieh, C., and Morris, P., "Comparison of Two- and Three-Dimensional Turbulent Cavity Flows," 39th AIAA Aerospace Sciences Meeting and Exhibit, AIAA Paper 2001-0511, Reno, NV, 8–11 Jan. 2001.

[27] Larchevêque, L., Sagaut, P., Mary, I., and Labbe, O., "Large-Eddy Simulation of a Compressible Flow Past a Deep Cavity," *Physics of Fluids*, Vol. 15, No. 1, 2003, pp. 193–210. doi:10.1063/1.1522379

[28] Nichols, R., Tramel, R., and Buning, P., "Solver and Turbulence Model Upgrades to OVERFLOW 2 for Unsteady and High-Speed Applications," 24th Applied Aerodynamics Conference, AIAA Paper 2006-2824, San Francisco, CA, 5–8 June 2006.

[29] Menter, F., "Two-Equation Eddy-Viscosity Turbulence Models for Engineering Applications," *AIAA Journal*, Vol. 32, No. 8, 1994, pp. 1598–1605. doi:10.2514/3.12149

[30] Wilcox, D., "Reassessment of the Scale-Determining Equation for Advanced Turbulence Models," *AIAA Journal*, Vol. 26, No. 11, 1988, pp. 1299–1310. doi:10.2514/3.10041

[31] Nichols, R., "Comparison of Hybrid Turbulence Models for a Circular Cylinder and a Cavity," *AIAA Journal*, Vol. 44, No. 6, 2006, pp. 1207–1219. doi:10.2514/1.17016

[32] Sanchez-Rocha, M., Kirtas, M., and Menon, S., "Zonal Hybrid RANS-LES Method for Static and Oscillating Airfoils and Wings," *Collection of Technical Papers: 44th AIAA Aerospace Sciences Meeting*, Vol. 20, 2006, pp. 15211–15231; also AIAA Paper 2006-1256, Reno, NV, 2006.

[33] Shelton, A., Braman, K., Smith, M., and Menon, S., "Improved Hybrid RANS-LES Turbulence Models for Rotorcraft," AHS 62nd Annual Forum, Phoenix, AZ, 9–11 May 2006.

[34] Baurle, R., Tam, C., Edwards, J., and Hassan, H., "Hybrid Simulation Approach for Cavity Flows: Blending, Algorithm, and Boundary Treatment Issues," *AIAA Journal*, Vol. 41, No. 8, 2003, pp. 1463–1480. doi:10.2514/2.2129.

[35] Fang, Y., and Menon, S., "A Two-Equation Subgrid Model for Large-Eddy Simulation of High Reynolds Number Flows," 44th AIAA Aerospace Sciences Meeting and Exhibit, AIAA Paper 2006-0116, Reno, NV, 9–12 Jan. 2006.

[36] Fang, Y., and Menon, S., "Kinetic-Eddy Simulation of Static and Dynamic Stall," 24th AIAA Applied Aerodynamics Conference, AIAA Paper 2006-3847, San Francisco, CA, 5–8 June 2006.

[37] Rossiter, J., "Wind-Tunnel Experiments on the Flow over Rectangular

Cavities at Subsonic and Transonic Speeds. Reports and Memoranda 3438," Aeronautical Research Council Rept. 3438, 1964.

[38] Burg, J., "Maximum Entropy Spectral Analysis," *Proceedings of the 37th Meeting of the Society of Exploration Geophysicists*, Oklahoma City, OK, 31 Oct. 1967.

[39] Burg, J., "A New Analysis Technique for Time Series Data," *Modern Spectrum Analysis*, edited by D. Childers, Institute of Electrical and Electronics Engineers, New York, 1978, pp. 42–48.

[40] Huang, L., and Ho, C., "Small-Scale Transition in a Plane Mixing Layer," *Journal of Fluid Mechanics*, Vol. 210, Jan. 1990, pp. 475–500.

[41] Larcheveque, L., Sagaut, P., Le, T., and Comte, P., "Large-Eddy Simulation of a Compressible Flow in a Three-Dimensional Open Cavity at High Reynolds Number," *Journal of Fluid Mechanics*, Vol. 516, Oct. 2004, pp. 265–301. doi:10.1017/S0022112004000709

[42] Cattafesta, L., III, Garg, S., Kegerise, M., and Jones, H., "Experiments on Compressible Flow-Induced Cavity Oscillations," 29th Fluid Dynamics Conference, AIAA Paper 1998-2912, Albuquerque, NM, 15–18 June 1998.

[43] Tucker, P., Menon, S., Merkle, C., Oefelein, J., and Yang, V., "Validation of High-Fidelity CFD Simulations for Rocket Injector Design," 44th AIAA/ASME/SAE/ASEE Joint Propulsion Conference and Exhibit, AIAA Paper 2008-5226, Hartford, CT, 21–23 July 2008.